

PAPER

Shearlet-based compressed sensing for fast 3D cardiac MR imaging using iterative reweighting

To cite this article: Jackie Ma *et al* 2018 *Phys. Med. Biol.* **63** 235004

View the [article online](#) for updates and enhancements.



PAPER

RECEIVED
8 April 2018REVISED
30 September 2018ACCEPTED FOR PUBLICATION
22 October 2018PUBLISHED
22 November 2018

Shearlet-based compressed sensing for fast 3D cardiac MR imaging using iterative reweighting

Jackie Ma^{1,7}, Maximilian März², Stephanie Funk^{3,6}, Jeanette Schulz-Menger^{3,6}, Gitta Kutyniok², Tobias Schaeffter^{4,5} and Christoph Kolbitsch^{4,5}

¹ Image and Video Coding Group, Fraunhofer Institute for Telecommunications—Heinrich Hertz Institute, Berlin, Germany

² Department of Mathematics, Technische Universität Berlin, Berlin, Germany

³ Department of Cardiology and Nephrology, HELIOS Klinikum Berlin Buch, Berlin, Germany

⁴ Physikalisch-Technische Bundesanstalt (PTB), Braunschweig and Berlin, Germany

⁵ School of Biomedical Engineering and Imaging Sciences, King's College London, London, United Kingdom

⁶ Working Group Cardiovascular Magnetic Resonance, Experimental and Clinical Research Center, a joint cooperation between the Charité Medical Faculty and the Max-Delbrück Center for Molecular Medicine.

⁷ Author to whom any correspondence should be addressed.

E-mail: jackie.ma@hhi.fraunhofer.de

Keywords: magnetic resonance imaging, compressive sensing, image reconstruction—iterative methods

Abstract

High-resolution three-dimensional (3D) cardiovascular magnetic resonance (CMR) is a valuable medical imaging technique, but its widespread application in clinical practice is hampered by long acquisition times. Here we present a novel compressed sensing (CS) reconstruction approach using shearlets as a sparsifying transform allowing for fast 3D CMR (3DShearCS) using 3D radial phase encoding (RPE). An iterative reweighting scheme was applied during image reconstruction to ensure fast convergence and high image quality. Shearlets are mathematically optimal for a simplified model of natural images and have been proven to be more efficient than classical systems such as wavelets. 3DShearCS was compared to three other commonly used reconstruction approaches. Image quality was assessed quantitatively using general image quality metrics and using clinical diagnostic scores from expert reviewers. The proposed technique had lower relative errors, higher structural similarity and higher diagnostic scores compared to the other reconstruction techniques especially for high undersampling factors, i.e. short scan times. 3DShearCS provided ensured accurate depiction of cardiac anatomy for fast imaging and could help to promote 3D high-resolution CMR in clinical practice.

1. Introduction

Magnetic resonance imaging (MRI) is a valuable medical imaging technique that can capture complex anatomical structures with excellent soft tissue contrast. This is especially important for cardiac applications such as the assessment of congenital heart disease or accurate treatment planning for image-guided percutaneous procedures.

The main challenge of high-resolution 3D cardiac MRI are long acquisition times. In order to achieve the necessary spatial resolution, MR data is obtained during free-breathing over multiple respiratory and cardiac cycles. Data acquisition is restricted to predefined respiratory (e.g. end-expiration) and cardiac (e.g. mid-diastole) phases to minimize motion artefacts. This approach provides high image quality but can lead to scan times of more than 15 min which makes it challenging to apply in clinical practice (Kolbitsch *et al* 2011, Pang *et al* 2014).

Several approaches have been proposed to reduce scan times by acquiring less data and utilizing additional information about the acquired data in the image reconstruction. Parallel imaging techniques for example use the spatial information from multiple receiver coils to improve the conditioning of the image reconstruction problem (Sodickson and Manning 1997, Pruessmann *et al* 1999, Griswold *et al* 2002). Further improvements in image quality can be achieved by applying the framework of compressed sensing to MR image reconstruction (Lustig *et al* 2008) and its combination with parallel imaging (Liang *et al* 2009, Uecker *et al* 2013). TV-based reconstruction techniques are frequently used in MR image reconstruction, for instance, in the context of parallel

imaging techniques this has been done in Block *et al* (2007). If the MR image itself or a transformation of the MR image is sparse, this sparsity can be used to suppress undersampling artefacts and improve image quality. In cardiovascular MRI, compressed sensing has been applied to a wide range of different techniques. Nakamura *et al* have shown improvement in coronary artery visualization in 3D coronary MRI using CS compared to standard image reconstruction (Nakamura *et al* 2018). In Forman *et al* (2014) the authors have studied high-resolution 3D whole-heart coronary MRA. Further, Vincenti *et al* have studied quantification of cardiac characteristics in CMR in Vincenti *et al* (2014) based on compressed sensing.

For 2D cine imaging (i.e. dynamic imaging of the heart during the cardiac cycle, compressed sensing has been used to exploit sparsity along the temporal direction in order to greatly reduce acquisition times and improve image quality (Jung *et al* 2009, Otazo *et al* 2010, Feng *et al* 2012). Combining sparsity transforms along the spatial and temporal direction for 4D and 5D imaging has also recently been shown to improve image quality for respiratory and/or cardiac resolved 3D cardiac MRI (Kido *et al* 2016, Feng *et al* 2017, Liu *et al* 2017a). Although there are other approaches such as dictionary learning (Ravishankar and Bresler 2011) or exploiting low-rank properties (Miao *et al* 2016), the majority of compressed sensing approaches in cardiovascular MRI use either wavelet or finite difference based sparsity transforms, which we will be focusing here.

Although the wavelet transform is very robust for a wide range of different images and applications, the wavelet transform is not necessarily optimal to accurately describe anatomical images of the heart. Recently, the shearlet transform has been proposed for medical image reconstruction (Ma 2017). The shearlet transform is based on a multiscale directional system that provides mathematically provable optimal approximation rates of so-called *cartoon-like functions* (Kutyniok and Lim 2011) which are a simplified model for images, in particular, medical images. Wavelets do not fulfill such an optimal approximation rate of curvi-linear singularities which represent the edges in an image. This favors the choice of shearlets in image reconstruction problems such as denoising and inpainting. The two main reasons why shearlets outperform wavelets in terms of the approximation rate of images is that shearlets are built upon anisotropic scaling and shearing. The latter allows the elements to have different directionalities. These two properties allow for elongated and directional elements which are much more adapted to curves than isotropic and non-directional elements such as for wavelets.

Previous studies have shown that shearlet-based compressed sensing (CS) approaches yield an improved MR image quality compared to wavelet-based reconstructions (Kutyniok and Lim 2016, Ma 2017). Nevertheless, so far these studies have only been carried out in 2D using simulated MR data of the brain. Data acquisition in these simulations was assumed to be Cartesian (i.e. each k-space point is located on a uniform grid) which strongly simplifies the image reconstruction process. In addition, the spatially varying sensitivity of receiver coils commonly used to record the MR signal was not taken into consideration in these studies.

In this paper we present a non-Cartesian 3D shearlet-based CS reconstruction approach which allows for the reconstruction of a single static 3D high-resolution image from MR data obtained on arbitrary k-space locations using multiple receiver coils. In this case the reconstruction operator is not easily diagonalizable anymore and requires an iterative solver. In addition, a 3D shearlet system is used to fully utilize the available spatial information. In order to ensure high image quality and achieve fast convergence, which is especially important for medical *in vivo* applications, a multi-level reweighting procedure is proposed. This reweighting scheme optimizes the weighting of the sparsity transform for a uniform treatment of sparsity structure across all levels. The 3D shearlet-based CS approach was evaluated on *in vivo* cardiac MR scans of five healthy volunteers. Image quality was assessed using general image quality metrics and clinical diagnostic scores.

2. Methods

2.1. MR acquisition model

In MRI, data is acquired in Fourier-space or k-space and the transform of the obtained k-space data y with n_k data points to the image data x of size $N^3 \times 1$ can be described with the encoding operator E

$$y = Ex = GFSx. \quad (1)$$

S describes the spatial distribution of the sensitivity of n_c receiver coils which are used to record the MR signal. It can be calculated from an additional calibration scan or from the image data itself. F is the Fourier operator and is commonly realized using a discrete fast Fourier transform (FFT). If the obtained k-space points are located on a Cartesian grid, G is simply a mask selecting the acquired data. For non-Cartesian acquisition schemes, G requires the interpolation of data points from arbitrary positions onto a cartesian grid (Jackson *et al* 1991). The dimensions of E are $n_c \times N^3$.

2.2. Compressed sensing

Compressed sensing (CS) has been introduced by Donoho (2006) and Candès *et al* (2005), Candès *et al* (2006) as a methodology that allows for successful reconstructions using considerably less information than other

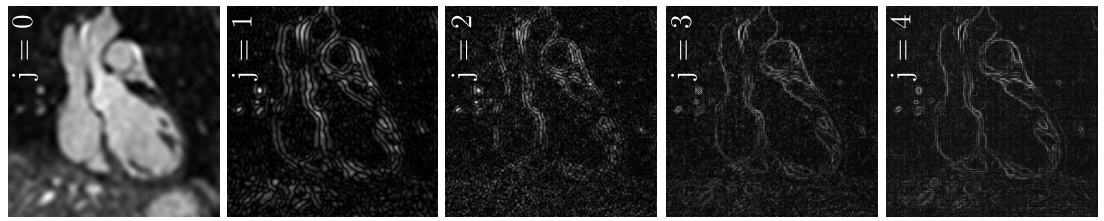


Figure 1. Shearlet coefficients at different scales ($j = 0, 1, 2, 3$ and 4). For better visualization the contrast has been adapted for each scale.

conventional methods such as the reconstruction formula given by the Shannon–Nyquist theorem (Shannon 1948). One of the key ideas is to incorporate randomness into the measurement process and solving an ℓ^1 -minimization problem of the form

$$\min_x \|x\|_1 \quad \text{subject to} \quad \|y - Ex\|_2 \leq \varepsilon, \quad (2)$$

where E denotes the encoding matrix that gives rise to the measured data y with an estimated accuracy $\varepsilon > 0$.

Problem (2) is known to have a unique sparse solution provided $E \in \mathbb{R}^{m \times N}$ satisfies certain properties such as the so-called *restricted isometry property* (Candès 2008). Moreover, one of the key assumptions is that the vector of interest $x \in \mathbb{R}^N$ is *sparse*, i.e. the number of non-zero elements

$$\#\{k \in \{1, \dots, N\} : x_k \neq 0\}$$

is small compared to N . However, in many applications the object of interest x is not directly sparse but only after the application of a suitable transform Ψ . This is, for example, the case in MR imaging. Hence, instead of solving (2), Lustig *et al* have considered

$$\min_x \|\Psi x\|_1 \quad \text{subject to} \quad \|y - Ex\|_2 \leq \varepsilon \quad (3)$$

for recovering MR data from highly undersampled data and a sparsifying transform Ψ (Lustig *et al* 2008). Theoretical results guaranteeing a solution for (3) are also available in the literature. This was first studied by Candès *et al* (2011) by extending the restricted isometry property to the so-called Ψ -restricted isometry property.

There are many different possible transforms for Ψ , with the *wavelet transform* (Daubechies 1992) being the most prominent one. Despite its common use, wavelet transforms do not necessarily provide an optimal description of MR images. As we have already mentioned in the introduction a multiscale directional transform, such as the *shearlet transform* (Lim 2010, 2013) can mathematically be shown to outperform the classical wavelet transform (Kutyniok and Labate 2012) in terms of its approximation rate. Figure 1 shows an example of the shearlet coefficients of a cardiac MR image. The approximation using wavelets and shearlets for MRI using uniform samples is discussed in Ma (2017).

In this work we will use a multi-level reweighting strategy together with the shearlet transform. The reweighting algorithm is not solely build for the shearlet transform but more generally for multilevel transform, which will be discussed in sections 2.3 and 2.4. In section 2.5 we will then present the 2D and 3D shearlet system.

2.3. Multilevel reweighting

The idea of using reweighting in order to improve solutions of (2) was first considered by Candès *et al* (2008). In order to enhance the sparsity of the recovered coefficients a weighting matrix $W = \text{diag}(\sigma_1, \dots, \sigma_N) = (\sigma_i \delta_{i,j})_{i,j \in \mathbb{N}}$ is introduced, where $\delta_{i,j} = 1$ if $i = j$ and 0 otherwise. Further, the weights $\sigma_i > 0$, $i = 1, \dots, N$ are adapted to the sparsity structure of the object of interest x^* . More precisely, suppose $x^* = (x_1^*, \dots, x_N^*) \in \mathbb{R}^N$ is the true signal that one wishes to recover. Then the minimization problem

$$\min_x \|Wx\|_1 \quad \text{subject to} \quad \|y - Ex\|_2 \leq \varepsilon \quad (4)$$

with weights

$$\sigma_i = \begin{cases} \frac{1}{|x_i^*|}, & x_i^* \neq 0 \\ \infty, & \text{otherwise,} \end{cases} \quad (5)$$

will ideally find sparser solutions than the unweighted minimization problem in (2) (Candès *et al* 2008). Note that the weights shown in (5) are practically not feasible as they already assume the knowledge of the true signal x^* that one wishes to recover. Hence, one usually considers a sequence of weights

$$\sigma_i^k = \frac{1}{|x_i^k| + \nu},$$

where $\nu > 0$ is small and $(x^k)_k \subset \mathbb{R}^N$ is a sequence of approximations to the true signal x^* obtained by

$$x^k = \operatorname{argmin}_x \|W^{k-1}x\|_1 \quad \text{subject to} \quad \|y - Ex\|_2 \leq \varepsilon. \quad (6)$$

Note that the weights defined in (6) penalize small coefficients stronger and thus contribute the information that they are more likely zero in the true signal. When adopting this idea to the minimization problem considered in (3), the straightforward implementation would yield weights of the form

$$\sigma_i^k = \frac{1}{|(\Psi x^k)_i| + \nu}, \quad (7)$$

where

$$x^k = \operatorname{argmin}_x \|W^{k-1}\Psi x\|_1 \quad \text{subject to} \quad \|y - Ex\|_2 \leq \varepsilon.$$

Although the coefficients computed from a multiscale transform can be sparse, they often intrinsically decrease due to the multiscaling, as it is for instance the case for the wavelet transform. In order to take full advantage of the reweighting scheme explained above, the natural decrease of the coefficients in magnitude has to be compensated for in order to avoid wrong classifications of zero coefficients. Otherwise the low scale coefficients would always be significantly more important, due to the larger coefficients, than high scale coefficients.

Here we have proposed the use of weights that are associated with levels $j \in \{1, \dots, J\}$ that correspond to the scales of the multiscale transform such as the wavelet transform and shearlet transform. The general idea of multilevel reweighting is now not to equally apply the classical reweighting across all levels but rather separately within each level. The resulting proposed weights are then

$$\sigma_{ij}^k = \frac{\lambda_j}{|(\Psi x^k)_i| + \nu}, \quad i \in \{N_{j-1} + 1, \dots, N_j\} \quad (8)$$

per level j and index sets $\{N_{j-1} + 1, \dots, N_j\}$ that partition the levels, i.e.,

$$\{1, \dots, N\} = \bigcup_{j=1}^J \{N_{j-1} + 1, \dots, N_j\}.$$

The choice of $(\lambda_j)_j$ is a very subtle problem. We have decided to use a adapt the weights to the maximum levels, that is

$$\lambda_j = \max \left\{ \left| \langle \psi_{j,l}, x^k \rangle \right| : l = N_j, \dots, N_{j+1} - 1 \right\}. \quad (9)$$

Note that $(\lambda_j)_j$ depend on the current iterate x^k . It is also possible to use quantiles over all coefficients per level. Further choices are for instance proposed in Ahmad and Schniter (2015). Note that this method is computationally very demanding especially for 3D images as (6) has to be solved many times. Note that the weights have to be stored and computed after each iteration.

2.4. Algorithm

The iterative reweighting can be directly incorporated into the *alternating direction method of multipliers* (ADMM) (Gabay and Mercier 1976, Eckstein and Bertsekas 1992) which is a key method to solve sparse regularized inverse problems such as the MR image reconstruction problem that we consider in this paper. ADMM has also been used in the context of MRI for image reconstruction, for instance, it has been used by Ramani and Fessler (2010, 2011) for 2D radial MRI using a total variation regularization term which is a popular choice in medical imaging. ADMM is used to solve an unconstrained problem by introducing auxiliary variables in order to reduce the original problem to subproblems which may be easier to solve.

For ADMM, consider

$$\min_x |\Psi x|_1 + \frac{\beta}{2} |y - Ex|_2^2,$$

which is equivalent to (3) for a suitably chosen parameter β . Then the resulting ADMM steps for solving the latter problem are

$$\begin{aligned} x^{k+1} &= \operatorname{argmin}_x \frac{\beta}{2} |y - Ex|_2^2 + \frac{\mu}{2} \|d - \Psi x - b^k\|_2^2, \\ d^{k+1} &= \operatorname{argmin}_d |d|_1 + \frac{\mu}{2} \|d - \Psi x^{k+1} - b^k\|_2^2, \\ b^{k+1} &= b^k + \Psi x^{k+1} - d^{k+1}, \end{aligned}$$

for a parameter $\mu > 0$. In order to solve the x -update, the system

$$(\beta E^* E + \mu \Psi^* \Psi) x = \beta E^* y + \mu \Psi^* (d^k - b^k) \quad (10)$$

has to be solved. Equation (10) is now a key equation and its solvability depends strongly on the mathematical properties of the operators. In fact, if the encoding operator E is simply given as a subsampled discrete Fourier transform, the matrix on the left hand side is diagonalizable by the discrete Fourier transform and therefore the system (10) is explicitly solvable in $\mathcal{O}(n \log n)$ flops.

For our non-Cartesian encoding operator E however, we propose to use an iterative method to solve the system approximately. It is known that ADMM still converges, although (10) is not solved up to full precision (Deng and Yin 2016). By using the solution of the previous iterate one can use a *warm start* so that only a few iteration steps of the iterative method are necessary for the entire algorithm to converge.

Note that by solving the d -problem we obtain the sparsifying transform coefficients. The idea of using the weights to obtain even sparser transform coefficients can be directly incorporated in this subproblem. Hence the multilevel adapted iterative reweighting steps are directly incorporated into the d -update as follows:

$$d^{k+1} = \operatorname{argmin}_d \|W^{k+1} d\|_1 + \frac{\mu}{2} \|d - \Psi x^{k+1} - b^k\|_2^2, \quad (11)$$

where the weighting matrix $W^{k+1} = \operatorname{diag}(\sigma_1^{k+1}, \dots, \sigma_n^{k+1})$ is given as in (8) by

$$\sigma_{ij}^{k+1} = \frac{\lambda_j}{|(\Psi x^k)_{ij}| + \nu}, \quad i_j \in \{N_{j-1} + 1, \dots, N_j\}, \quad (12)$$

and $(\lambda_j)_j$ are as in (9). The proximal step (11) is then explicitly solved by

$$d^{k+1} = \operatorname{shrink}\left(\Psi x^{k+1} + b^k, \frac{1}{\mu} W\right),$$

where

$$\operatorname{shrink}(z, \lambda) = \begin{cases} \max(|z| - \lambda, 0) \frac{z}{|z|}, & z \neq 0 \\ 0, & z = 0 \end{cases}$$

is applied element-wise.

Algorithm 1. Proposed 3D Shear-CS algorithm with iterative reweighting.

Input:

Encoding operator E , multilevel transform Ψ , regularization parameters: $\alpha_0, \alpha_1, \mu_1, \mu_2, \mu_3, \beta$, iteration numbers N and maxIter.

Data:

Measured data y .

Initialization:

$k \leftarrow 0$;

$x_0 \leftarrow e^* y$;

$y_0, b_0, d_0^w \leftarrow 0$;

while $k \leq \text{maxIter}$ **do**

for $i = 1, \dots, N$ **do**

$x_{k+1} \leftarrow \text{solve linear system (10)}$;

for $j = 1, \dots, J$ **do**

$\lambda_j = \max \{ |\langle \psi_{j,l}, x^{\text{cur}} \rangle| : l = N_j, \dots, N_{j+1} - 1 \}$;

$W_j = \operatorname{diag}\left(\frac{\lambda_j}{\varepsilon + |\langle \psi_{j,l}, x^{\text{cur}} \rangle|}\right)$;

for $l = 1, \dots, N_j$ **do**

$d^{k+1}(l) \leftarrow \operatorname{shrink}\left((\Psi_j x^{\text{cur}})(l) + d^k(l), \frac{W_j(l)}{\mu_1}\right)$

end for;

end for

end for

$b^{k+1} \leftarrow b^k + \Psi x^{k+1} - d^{k+1}$;

$y_{k+1} \leftarrow y_k + y - A u_{k+1}$;

$k \leftarrow k + 1$;

end while

return Reconstruction u_{maxIter} .

2.5. Shearlets

Shearlet systems were first introduced by Labate *et al* (2005), Guo *et al* (2006) and Lim (2010) as a directional representation system that provably outperforms classical systems such as wavelets within a certain model. The model assumption is that the function that is to be approximated is a so-called *cartoon-like function*. These are functions that are smooth up to a smooth discontinuity curve. These functions serve as a model for natural images. It is known that wavelets, for instance, can only provide a best N -term approximation rate of the order N^{-1} while shearlets do, up to log factors, reach N^{-2} (Kutyniok and Lim 2011, Kutyniok and Labate 2012) which is optimal for this class of functions (Donoho 2001). Moreover, similar to wavelets a construction using compactly supported generators can also be obtained which in turn allows fast implementations (Kittipoom *et al* 2012).

The novelty of this system compared to classical wavelet systems are the parabolic scaling matrices

$$A_{2^j} = \begin{pmatrix} 2^j & 0 \\ 0 & 2^{j/2} \end{pmatrix}, \quad \tilde{A}_{2^j} = \begin{pmatrix} 2^{j/2} & 0 \\ 0 & 2^j \end{pmatrix}, \quad j \geq 0$$

and the shear matrix

$$S_k = \begin{pmatrix} 1 & k \\ 0 & 1 \end{pmatrix}, \quad k \in \mathbb{Z}.$$

These matrices are used in the following definition of a *shearlet system*.

Definition 2.1 (Kittipoom *et al* (2012)). Let $\phi, \psi, \tilde{\psi} \in L^2(\mathbb{R}^2)$ be the *generating functions* and $c = (c_1, c_2) \in \mathbb{R}^+ \times \mathbb{R}^+$. Then the (*cone adapted discrete*) *shearlet system* is defined as

$$\mathcal{SH}(\phi, \psi, \tilde{\psi}, c) = \Phi(\phi, c_1) \cup \Psi(\psi, c) \cup \tilde{\Psi}(\tilde{\psi}, c),$$

where

$$\begin{aligned} \Phi(\phi, c_1) &= \{\phi(\cdot - c_1 m) : m \in \mathbb{Z}^2\}, \\ \Psi(\psi, c) &= \left\{ \psi_{j,k,m} : j \geq 0, |k| \leq 2^{j/2}, m \in \mathbb{Z}^2 \right\}, \\ \tilde{\Psi}(\tilde{\psi}, c) &= \left\{ \tilde{\psi}_{j,k,m} : j \geq 0, |k| \leq 2^{j/2}, m \in \mathbb{Z}^2 \right\}, \end{aligned}$$

and

$$\begin{aligned} \psi_{j,k,m} &= 2^{3j/4} \psi((S_k A_{2^j}) \cdot -cm), \\ \tilde{\psi}_{j,k,m} &= 2^{3j/4} \tilde{\psi}((S_k^T \tilde{A}_{2^j}) \cdot -cm). \end{aligned}$$

The multiplication of c and $\tilde{c} = (c_2, c_1)$ with the translation parameter m should be understood entry wise.

The parabolic scaling yield elongated supports of the shearlet functions, whereas the shear matrix introduces a directionality of the shearlet functions.

The attentive reader might wonder, why a shear action is used to obtain a directional component and not, for instance, rotation. Indeed, rotation has been used before shearing yielding the well-known *curvelets* by Candès and Donoho (2002). However, rotation does not leave the integer grid invariant which is particularly desired when implementing these systems.

Definition 2.1 concerns the case of 2D shearlets. Although we will also use these systems in this paper, our main purpose of study is 3D data. For such, one could use 2D shearlets on an image by image basis. However, as we will show, 3D shearlets yield better results because they fully utilize the 3D image information. The definition of 3D shearlets is a straightforward generalization of 2D shearlets (Kutyniok *et al* 2012, 2016) and we shall only give a brief presentation in this paper. The scaling matrices used for the 3D system are

$$\begin{aligned} A_{2^j} &= \begin{pmatrix} 2^j & 0 & 0 \\ 0 & 2^{j/2} & 0 \\ 0 & 0 & 2^{j/2} \end{pmatrix}, \quad \tilde{A}_{2^j} = \begin{pmatrix} 2^{j/2} & 0 & 0 \\ 0 & 2^j & 0 \\ 0 & 0 & 2^{j/2} \end{pmatrix}, \\ \hat{A}_{2^j} &= \begin{pmatrix} 2^{j/2} & 0 & 0 \\ 0 & 2^{j/2} & 0 \\ 0 & 0 & 2^j \end{pmatrix}, \quad j \geq 0, \end{aligned}$$

and the shear matrices are

$$S_k = \begin{pmatrix} 1 & k_1 & k_2 \\ 0 & 1 & 0 \\ 0 & 0 & 1 \end{pmatrix}, \quad \tilde{S}_k = \begin{pmatrix} 1 & 0 & 0 \\ k_1 & 1 & k_2 \\ 0 & 0 & 1 \end{pmatrix},$$

$$\hat{S}_k = \begin{pmatrix} 1 & 0 & 0 \\ 0 & 1 & 0 \\ k_1 & k_2 & 1 \end{pmatrix}, \quad k_1, k_2 \in \mathbb{Z}.$$

Using these 3×3 matrices once can extend the idea of cone adapted shearlets to the so-called *pyramid adapted shearlets*.

Definition 2.2 (Kutyniok et al (2012)). Let $\phi, \psi, \tilde{\psi}, \hat{\psi} \in L^2(\mathbb{R}^3)$ be the *generating functions* and $c = (c_1, c_2, c_3) \in \mathbb{R}^+ \times \mathbb{R}^+ \times \mathbb{R}^+$. Then the (*pyramid adapted discrete*) *shearlet system* is defined as

$$\mathcal{SH}(\phi, \psi, \tilde{\psi}, \hat{\psi}, c) = \Phi(\phi, c_1) \cup \Psi(\psi, c) \cup \tilde{\Psi}(\tilde{\psi}, c) \cup \hat{\Psi}(\hat{\psi}, c),$$

where

$$\Phi(\phi, c_1) = \{\phi(\cdot - c_1 m) : m \in \mathbb{Z}^3\},$$

$$\Psi(\psi, c) = \left\{ \psi_{j,k,m} : j \geq 0, |k_1|, |k_2| \leq 2^{j/2}, m \in \mathbb{Z}^3 \right\},$$

$$\tilde{\Psi}(\tilde{\psi}, c) = \left\{ \tilde{\psi}_{j,k,m} : j \geq 0, |k_1|, |k_2| \leq 2^{j/2}, m \in \mathbb{Z}^3 \right\},$$

$$\hat{\Psi}(\hat{\psi}, c) = \left\{ \hat{\psi}_{j,k,m} : j \geq 0, |k_1|, |k_2| \leq 2^{j/2}, m \in \mathbb{Z}^3 \right\},$$

and

$$\psi_{j,k,m} = 2^j \psi((S_k A_{2^j}) \cdot -cm),$$

$$\tilde{\psi}_{j,k,m} = 2^j \tilde{\psi}((\tilde{S}_k \tilde{A}_{2^j}) \cdot -\tilde{c}m),$$

$$\hat{\psi}_{j,k,m} = 2^j \hat{\psi}((\hat{S}_k \hat{A}_{2^j}) \cdot -\tilde{c}m).$$

The multiplication of c and $\tilde{c} = (c_2, c_1)$ with the translation parameter m should be understood entry wise.

3. Experiments

The shearlet-based CS image reconstruction approach was assessed in 3D *in vivo* cardiac MR images where we have used the toolbox for shearlets made available at www.shearlab.org. The performance of CS-based image reconstruction schemes depends strongly on the undersampling properties of the obtained MR data. To ensure high image quality, MR data has to be acquired in a way such that undersampling artefacts lead to incoherent signal contributions. Therefore, experiments were carried out with a radial phase encoding (RPE) MR sampling scheme. RPE has been shown previously to provide 3D high-resolution images even for high undersampling factors (Boubertakh et al 2009, Kolbitsch et al 2011). The RPE sampling scheme also allows for retrospective undersampling and simulation of different MR scan times.

3.1. MR data acquisition

3D whole-heart MR data was acquired with a balanced steady state free precession sequence to ensure optimal MR signal strength. Fat suppression and a T2 preparation pulse ($TE = 50$ ms) was applied to enhance image contrast. Sequence parameters were: field of view of $288 \times 288 \times 288$ mm 3 with an isotropic resolution of 1.5 mm 3 , flip angle of 90° and repetition/echo times of 4.3/2.2 ms. This acquisition provided high contrast between myocardium and blood to allow for accurate anatomical diagnosis of complex cardiac structures.

RPE is a Cartesian acquisition scheme with phase encoding carried out along radial lines in the 2D phase encoding plane ($PE_y - PE_z$). The angle between neighbouring RPE lines is constant and the sampling order of the angles was calculated using a bit-reversed scheme. Along each RPE line a partial Fourier factor of 0.75 was applied leading to 144 frequency encoding lines for each RPE line. 64 RPE lines were obtained leading to an undersampling factor of 4 compared to a fully sampled Cartesian acquisition. Figure 2 gives an overview of this sampling scheme. The acquisition was carried out in a sagittal orientation, with the readout (RO) along the foot-head direction and the 2D phase encoding plane in the transversal plane (figures 2(b) and (c)). Image reconstruction was carried out offline using Matlab (The MathWorks, Inc., Natick, MA, USA). The coil sensitivity information was calculated from the data itself based on reconstructing low-resolution images by applying

a low-pass k-space filter to the 2D phase-encoding plane. Homodyne weighting was used to compensate for the partial Fourier acquisition by applying a ramp function to each RPE line. Symmetrically acquired data in the centre of k-space is weighted by a factor of one and asymmetrically sampled data is weighted by a factor of two to compensate for the missing high-frequency k-space samples. The transition between the two regions was smoothed (Kolbitsch *et al* 2011).

The obtained data was retrospectively undersampled by a factor of 1, 2, 2.5, 3, 4 and 6 leading to images with a total undersampling factor (R) of 4, 8, 10, 12, 16 and 24 equivalent to average scan times of 12.6 min, 6.3 min, 5 min, 4.1 min, 3.2 min and 1.6 min. For RPE the k-space center is obtained for each phase encoding line. During the scan each RPE line is fully acquired before moving on to the next angle. The angles are obtained in a bit-reversed way, i.e. at 0° , 90° , 45° and so on. Therefore, realistic undersampling can be achieved, by simply restricting image reconstruction to the first N_R acquired RPE lines.

3.2. Image reconstruction

Each data set was reconstructed using

- a non-Cartesian iterative SENSE reconstruction technique (itSENSE) (Pruessmann *et al* 2001)
- a non-Cartesian iterative SENSE approach with a spatial total-variation constraint (TV) (Block *et al* 2007, Cruz *et al* 2016)
- a 3D wavelet-based CS method (WaveCS)
- the proposed 3D iteratively reweighted shearlet-based CS approach (3DShearCS)

WaveCS was implemented in the same framework as 3DShearCS to correspond to classical wavelet based MR image reconstructions using a decimated 3D wavelet transform without adaptive reweighting but classical ℓ^1 -minimization as proposed in Lustig *et al* (2008).

For comparison purposes images were also reconstructed with a 2D Shearlet system (2DShearCS) and a 3D shearlet system but without reweighting (3DShearCSnRW). For the 2D reconstruction, a 2D shearlet system was used on a 2D image by image basis in the transversal orientation as described in definition 2.1. For 3DShearCS-nRW the same algorithm was used as for 3DShearCS but without the adaptive reweighting method.

3.3. In vivo experiments

Five healthy volunteers were imaged on a 1.5 T MRI scanner (Philips Medical Systems, Best, The Netherlands) using a 32-channel cardiac phased array coil. Respiratory phase ordering with automatic window selection with a bin width of 3 mm and cardiac end-diastolic triggering were used to minimize respiratory and cardiac motion artefacts, respectively (Kolbitsch *et al* 2011). That ensured a single 3D imaging volume at a certain respiratory and cardiac phase with minimized motion artefacts. Written informed consent was obtained from all participants in accordance with the ethical rules of our institution.

3.4. Performance of 3D shearlet system

In order to successfully apply the proposed approach in clinical practice, reconstruction times also need to be kept at a minimum. The reconstruction times of the shearlet CS method are strongly determined by the total number of iterations and how often the weights are recalculated. We therefore evaluated the convergence of the reconstruction algorithm and the relative change of the weights for different iteration numbers for $R = 4, 8, 16$ and 24.

In order to assess the performance of a 3D shearlet system compared to a 2D shearlet system we reconstructed images for $R = 4, 8, 10, 12, 16$ and 24 for one volunteer using 2DShearCS.

3.5. Evaluation of image quality

We used two image error measurements namely the *relative error* and the *Haar wavelet-based perceptual similarity index (HaarPSI)*, Reisenhofer *et al* (2018).

The relative error is a standard measure and can be calculated using

$$\frac{\|x_{\text{ref}} - x_{\text{rec}}\|_2}{\|x_{\text{ref}}\|_2},$$

where x_{ref} is the vectorized reference image, x_{rec} is the vectorized reconstruction. Its value is dependent on the image content, making it difficult to compare between different volunteers with varying anatomy. Obviously a smaller number is preferred for the relative error and the relative error can easily be computed for 3D images.

The HaarPSI on the other hand is supposed to simulate the human similarity perception of objects in 2D and is therefore calculated on individual 2D slices. Hence, we have averaged the HaarPSI along all slices along the left-right direction. This choice is arbitrary and could be replaced by any other slice-direction. For HaarPSI

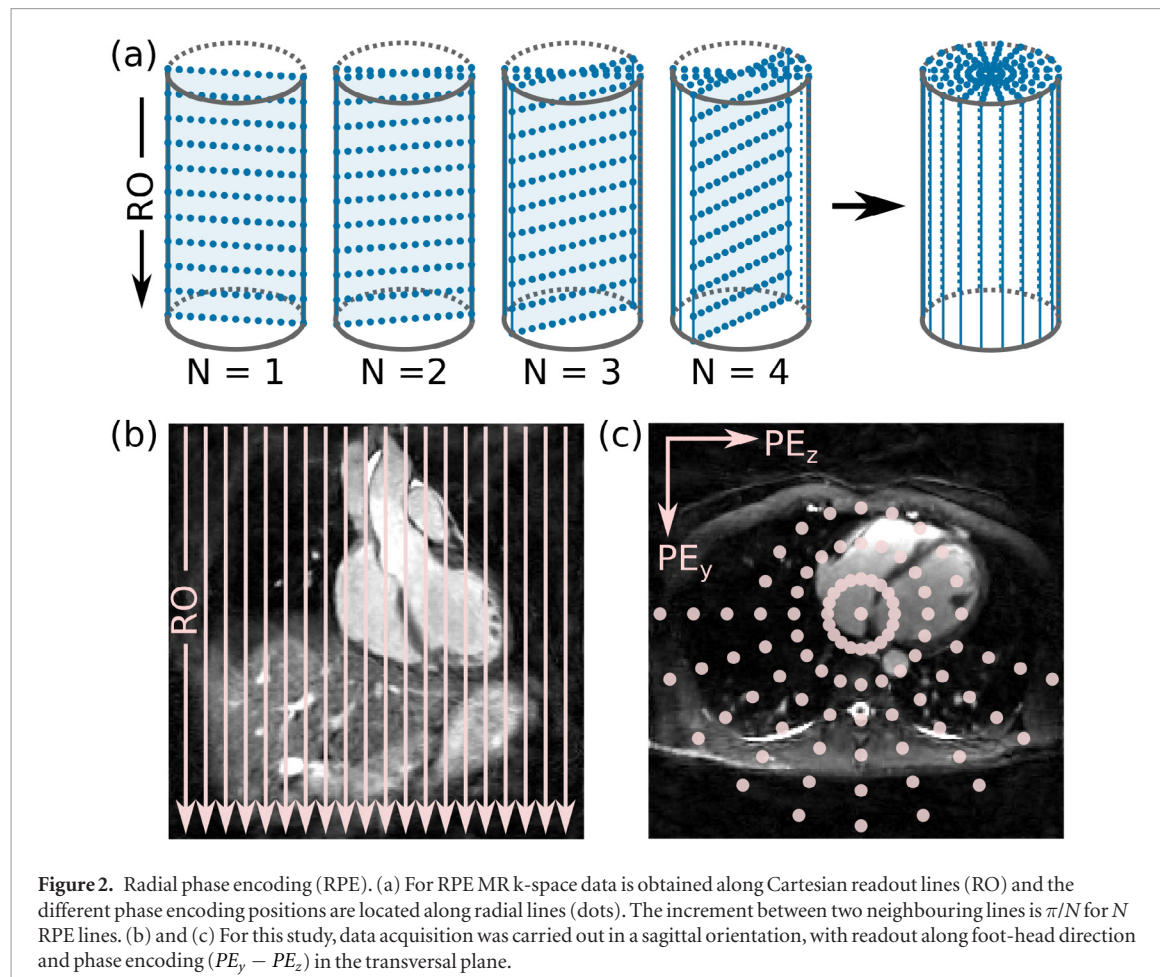


Figure 2. Radial phase encoding (RPE). (a) For RPE MR k-space data is obtained along Cartesian readout lines (RO) and the different phase encoding positions are located along radial lines (dots). The increment between two neighbouring lines is π/N for N RPE lines. (b) and (c) For this study, data acquisition was carried out in a sagittal orientation, with readout along foot-head direction and phase encoding ($PE_y - PE_z$) in the transversal plane.

the algorithm computes Haar wavelet coefficients to determine local similarities between two input images. The resulting index is a number between zero and one where a larger numbers represent a stronger similarity between two images. In Reisenhofer *et al* (2018) the method has been tested intensively on data bases where images have been scored by humans and in almost all cases HaarPSI has outperformed other common state of the art similarity indices. We refer the interested reader to that work and the references therein.

The quality of the obtained images was also assessed by measuring the sharpness (VS) of the coronary arteries. The MR data acquisition used in this study was optimised for 3D whole-heart visualization and not for coronary artery (CA) imaging. Nevertheless, the root of the CA was visible in all volunteers and hence could be used for analysis. The CA are small and complex structures with a diameter of approximately 3 mm (Piccini *et al* 2014) and are highly susceptible to undersampling artefacts. Therefore, they provide a sensitive metric on the quality of the reconstructed images. VS is calculated as the mean intensity of the vessel edges relative to the maximum intensity in the center of the vessel. A value of 1 corresponds to a very well defined vessel and a value of 0 means that the vessel could not be distinguished from the surrounding tissue, i.e. is not visible anymore. The assessment was carried out semi-automatically with a commercial tool developed for MR angiography (Etienne *et al* 2002).

In addition, the *in vivo* MR images were assessed by two clinical experts. They assessed if the images were of diagnostic quality (i.e. if the coronary arteries were visible), scored the images on a 3-point score (0 non-diagnostic; 1 good; and 2 excellent) and also selected the image which fitted best to a reference image for each under-sampling factor and volunteer separately. The whole assessment was performed with blinded reconstructions, meaning the two experts did not know which reconstruction corresponded to which method. If several images were equally comparable to the reference, multiple nominations were used. This scoring method has also been applied in Prothmann *et al* (2016).

All evaluations were carried out relative to a reference image. For *in vivo* acquisitions it was not possible to obtain a fully sampled k-space due to long acquisition time not feasible in practice. Therefore, images reconstructed with itSENSE from the original data with $R = 4$ were used as reference images. The evaluations were carried out using Matlab and R and statistical significance was determined with a two sampled *t*-test with a *p*-value smaller than 0.05 considered statistically significant.

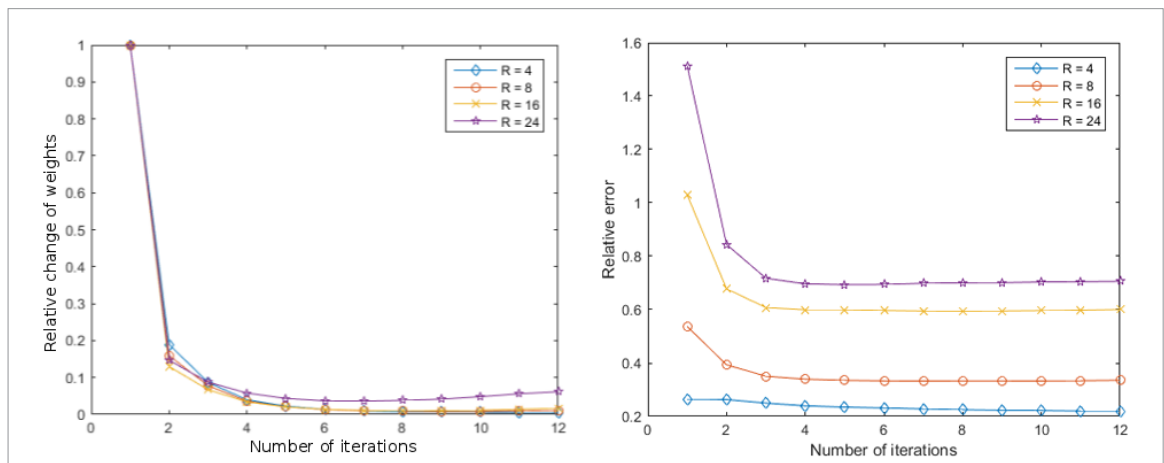


Figure 3. Relative change of weights (λ_j) and relative error per iteration of the proposed 3DShearCS method for different undersampling factors.

4. Results

4.1. Performance of 3D shearlet image reconstruction

Figure 3 shows the relative changes of the weights and relative error of the reconstruction at each iteration. Already after three iterations the relative change of the weights is less than 10%. It can be observed that for all undersampling factors $R = 4, 8, 16$ and 24 the algorithm converges quickly after a few iterations. It is also important to mention that we have not changed the parameters β and μ for the different undersampling rates which is usually needed for other methods that do not involve any adaptivity.

Based on these results we keep the weights fixed after three iterations and limit the total number of iterations to 12 to minimize reconstruction times.

Figure 4 shows the comparison between 3DShearCS, the image by image 2DShearCS reconstruction, and 3DShearCSnRW which can be referred to as a classical CS-MRI reconstruction using a shearlet regularizer. In particular, 3DShearCSnRW uses the same algorithm as 3DShearCS but without the additional reweighting. The 3D approach removes the artefacts significantly better than the 2D image reconstruction method 2DShearCS and the 3D reconstruction method without reweighting, that is 3DShearCSnRW. This becomes especially evident for higher undersampling factors. 2DShearCS does not utilize any information along the third image dimension (in our case foot-head direction) and thus does not take advantage of the full 3D data. The additional degree of freedom of the 3D shearlet system allows for a better distinction between undersampling artefacts and anatomical structures and hence lead to a higher image quality. On the other hand 3DShearCS suppresses the undersampling artefacts that are strongly visible in 3DShearCSnRW, the same 3D image reconstruction technique but without reweighting.

The quantitative image quality parameters vessel sharpness, HaarPSI, SSIM, PSNR, and the relative error are shown in figure 5. For $R > 4$ all quantitative measures confirm the higher image quality of the proposed 3DShearCS approach compared to 2DShearCS and 3DShearCSnRW.

4.2. *In vivo* evaluation

Figure 6 shows image reconstructed with four different reconstruction algorithms: itSENSE, WaveCS, TV and 3DShearCS for $R = 10, 12, 16$ and 24 and compares these images to the reference image obtained with itSENSE for $R = 4$. Higher undersampling factors lead to a higher degree of incoherent undersampling artefacts. TV and 3DShearCS achieve better minimization of these artefacts than itSENSE and WaveCS, especially for larger undersampling artefacts. Nevertheless, TV also shows regularisation artefacts leading to jagged rather than smooth edges of the anatomy. This becomes especially visible around small anatomical details, such as the papillary muscles and for $R > 12$. 3DShearCS on the other hand yields anatomically more accurate depiction of the cardiac anatomy. This is also confirmed for two other volunteers shown in figure 7 for $R = 12$. Small features such as the papillary muscles in the right ventricle are more accurately depicted using 3DShearCS than TV compared to the reference itSENSE with $R = 4$.

Figures 8 and 9 depict reformatted images showing the right and left coronary artery. For moderate degrees of undersampling WaveCS yields high image quality but for $R > 4$ it does not perform significantly better than standard itSENSE. TV is more robust towards undersampling artefacts but again shows regularisation artefacts which are avoided with the proposed 3DShearCS approach.

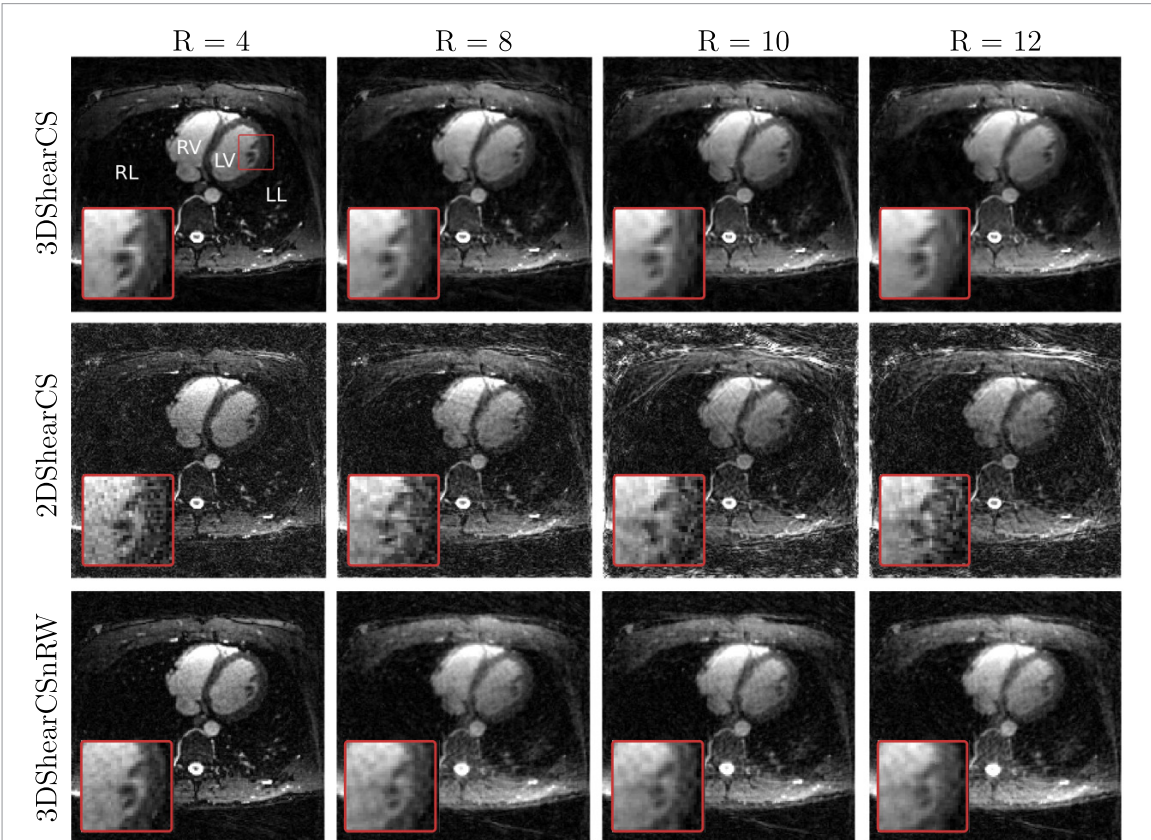


Figure 4. A reconstructed image along the foot-head-direction using 3DShearCS, 2DShearCS and 3DShearCSnRW for different undersampling factors $R = 4, 8, 10$, and 12 . Small anatomical features such as the papillary muscles in the left ventricle (small insert) are still visible for $R = 12$ using 3DShearCS but are difficult to distinguish from undersampling artefacts with 2DShearCS. RV right ventricle, LV left ventricle, RL right lung, LL left lung. For a better visualization the image contrasts were changed.

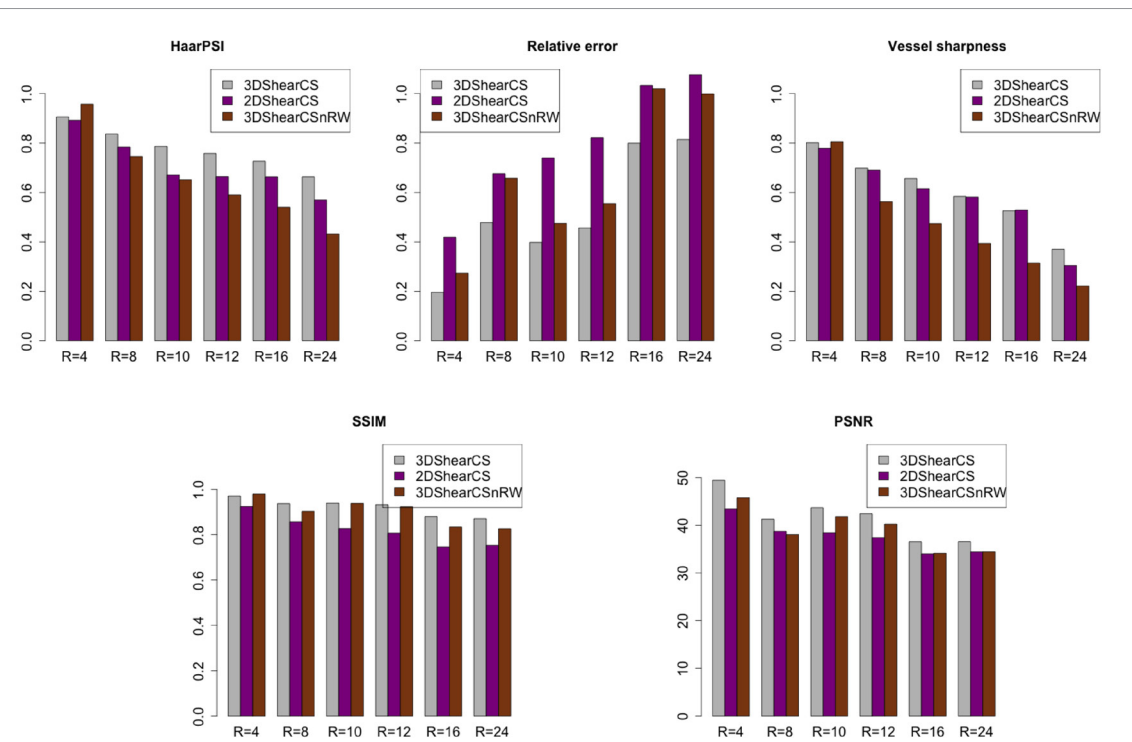


Figure 5. HaarPSI, relative error, vessel sharpness, SSIM and PSNR for image reconstructions using 3DShearCS, 2DShearCS, and 3DShearCSnRW for undersampling factors $R = 4, 8, 10, 12, 16$, and 24 .

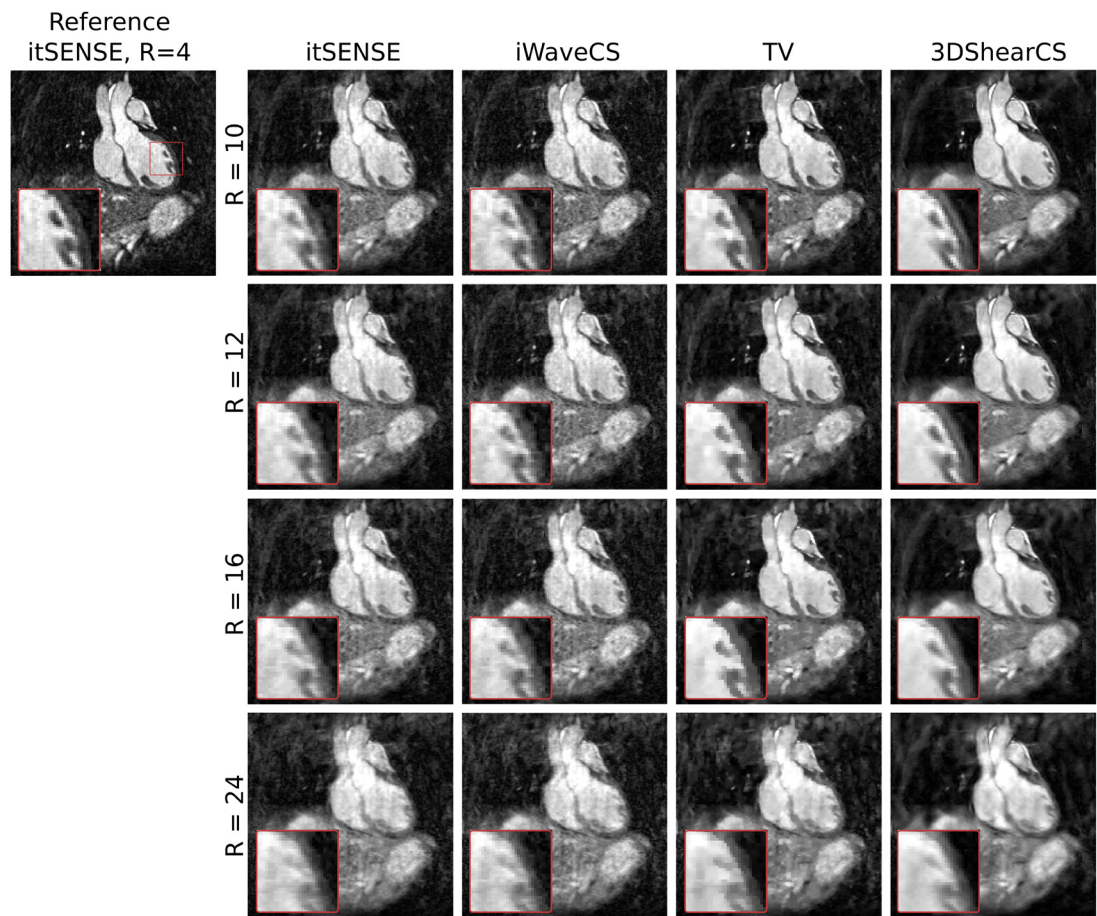


Figure 6. Comparison of all four reconstruction schemes for a undersampling factor $R = 10, 12, 16$ and 24 in one patient. 3DShearCS provides accurate anatomical depiction especially of small features such as the papillary muscles (small insert) most similar to the itSENSE reference image with $R = 4$.

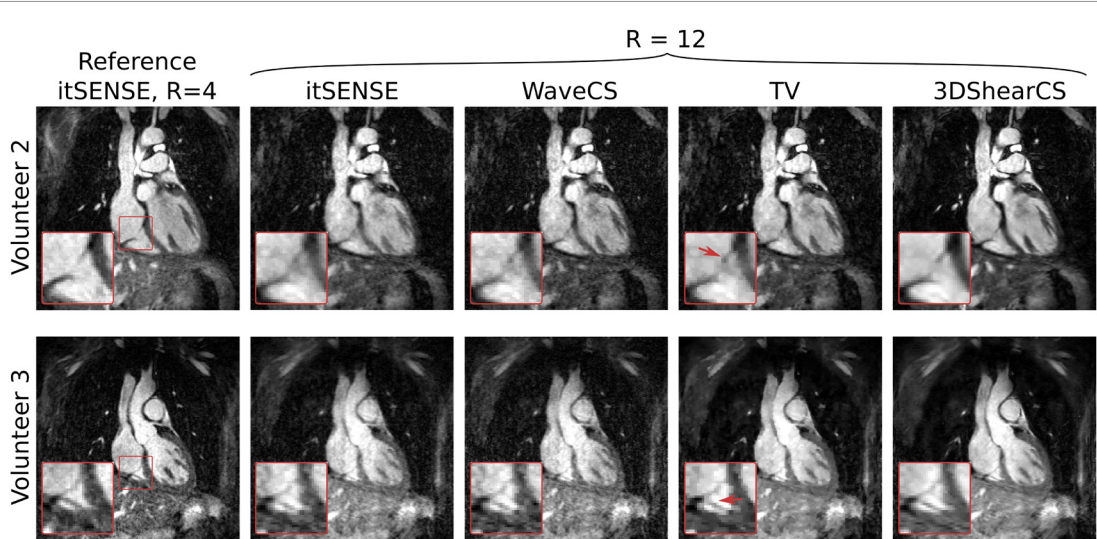


Figure 7. Comparison of all four reconstruction schemes for a undersampling factor of 12 for two patients. 3DShearCS provides a more accurate depiction of the anatomy especially of small features such as the papillary muscles in the right ventricle (small insert) compared to the reference image reconstruction. Although TV efficiently minimizes undersampling artefacts, it also leads to a patch-like visualisation of small image features (red arrows) which is avoided when using the proposed 3DShearCS approach.

The results of the quantitative assessment of the image quality are summarized in figure 10 and are in agreement with the above assessment. WaveCS performs worse than 3DShearCS and TV but yields similar results as itSENSE. 3DShearCS leads to superior image quality than the other approaches. For $R = 24$ 3DShearCS leads to superior image quality than the other approaches with improvements in vessel sharpness of $42\% \pm 28\%$

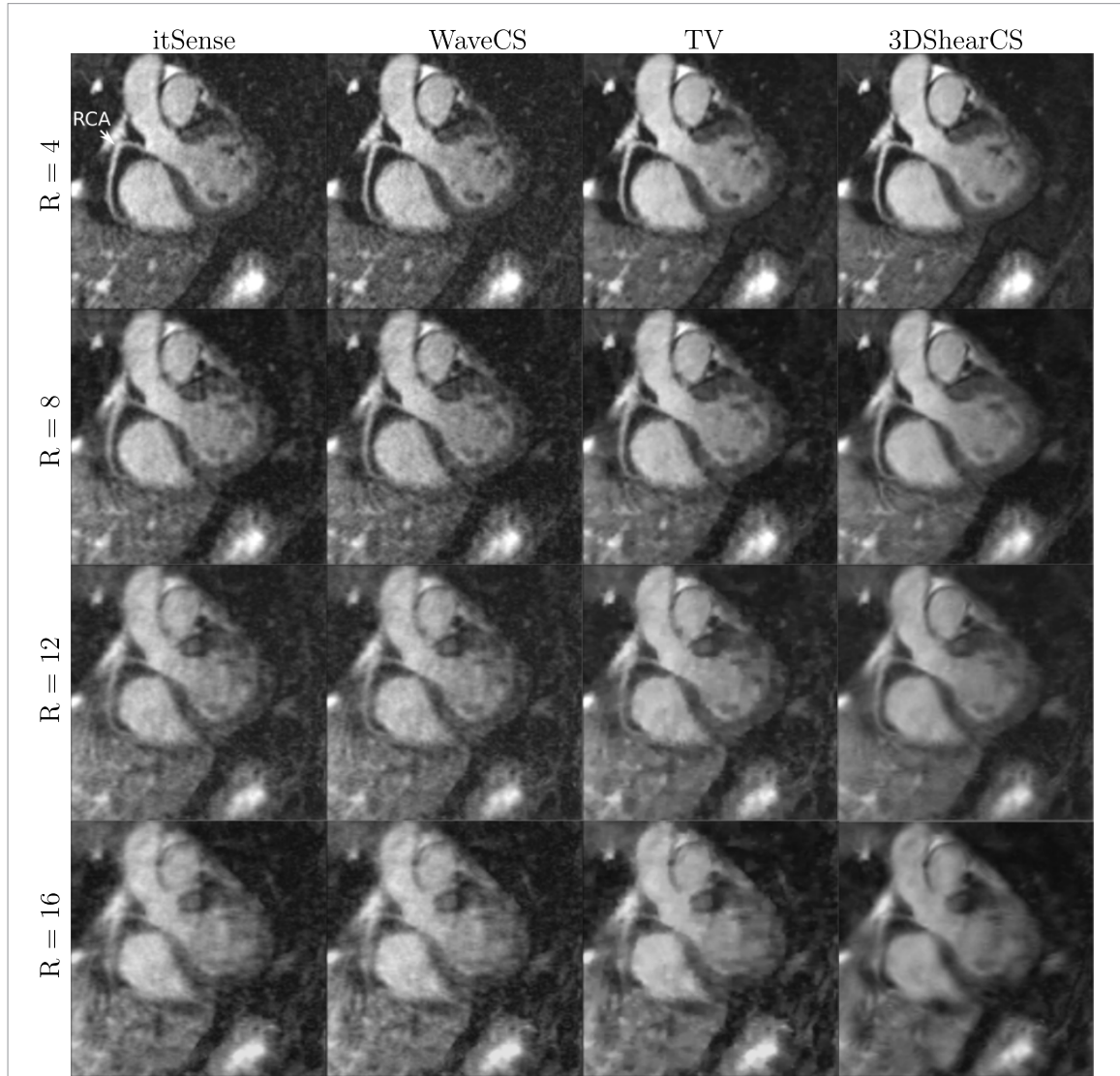


Figure 8. Reformatted images showing the right coronary artery (RCA) in a healthy volunteer for different undersampling factors and different reconstruction techniques. The proposed 3DShearCS approach ensures high image quality and good anatomical depiction for undersampling factors up to 12. For undersampling factor 16 the artefacts become stronger visible.

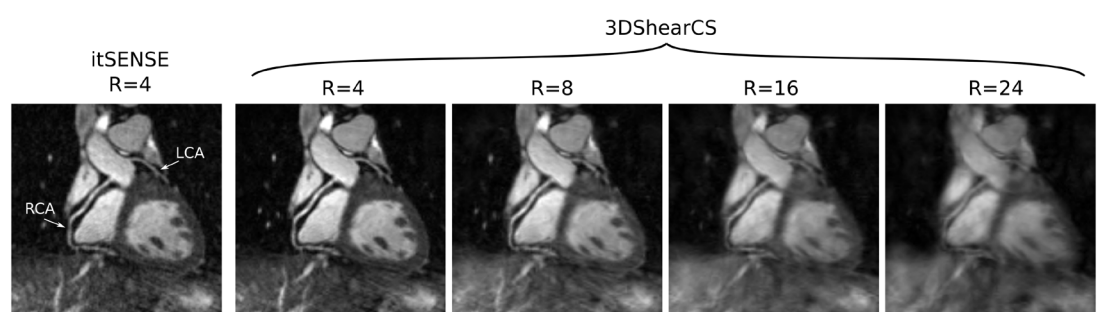
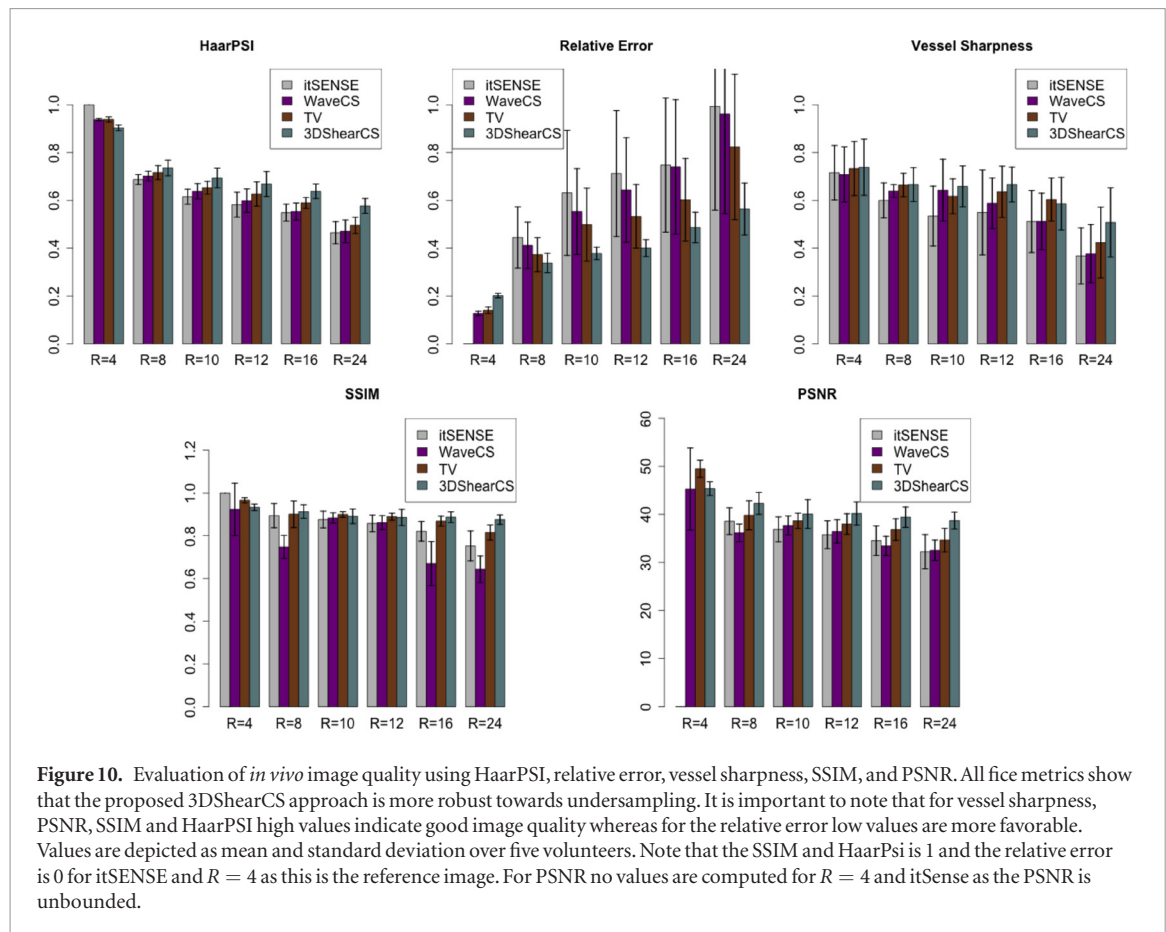


Figure 9. Reformatted images showing the right and left coronary artery (RCA/LCA) in a healthy volunteer comparing 3DShearletCS for different undersampling factors to the itSENSE reference for $R = 4$. The proposed 3DShearCS approach ensures high image quality and good anatomical depiction for undersampling factors up to 12. For undersampling factor 16 the artefacts become stronger visible and for $R = 24$ the visualisation of the cardiac anatomy is strongly impaired.

($p = 0.014$) compared to itSENSE, $39\% \pm 34\%$ ($p = 0.022$) compared to WaveCS and $23\% \pm 24\%$ ($p = 0.033$) compared to TV. HaarPsi and relative error show similar behavior with a reduction in RE of $37\% \pm 19\%$ compared to itSENSE ($p = 0.004$), $35\% \pm 18\%$ ($p = 0.005$) compared to WaveCS, $27\% \pm 15\%$ ($p = 0.002$) compared to TV and an improvement of $25\% \pm 11\%$ ($p = 0.042$) in HaarPsi compared to itSENSE, $23\% \pm 11\%$ ($p = 0.045$) compared to WaveCS, $17\% \pm 6\%$ ($p = 0.041$) compared to TV.



The clinical experts assessed 20 different reconstructions (five volunteers \times four different undersampling factors ($R = 4, 8, 16, 24$)) and compared the four different reconstruction methods to each other and to a reference image which was chosen as itSENSE with $R = 4$ (table 1). Reviewer 1 and Reviewer 2 scored a similar number of reconstructions to be of diagnostic quality, with non-diagnostic images occurring only for $R = 16$ and 24. The proposed 3DShearCS approach was scored with the highest image score by both reviewers, and images reconstructed with 3DShearCS agreed best with the reference image in the majority of cases.

5. Discussion

The proposed 3DShearCS approach was demonstrated to yield a better image quality than itSENSE, WaveCS and TV for a given undersampling factor. We have shown that extending the shearlet system from 2D to 3D leads to a better suppression of undersampling artefacts. The proposed iterative reweighting scheme ensures fast convergence and high image quality.

With increasing undersampling the image quality decreases for all methods, because less data and hence less information is available for image reconstruction. Nevertheless, for a given undersampling factor the overall performance of the proposed 3DShearCS approach is superior to the other reference methods. Even for an undersampling factor of 16, the image quality of 3DShearCS was assessed as sufficient for clinical diagnosis in all but one case by our clinical experts. For $R = 24$ image quality is strongly impaired and sever undersampling artefacts are visible.

The majority of previous studies on Shearlet-based CS reconstructions evaluated their proposed algorithms on synthetic 2D data, which was created by applying FFT to existing 2D MR image data. Although this approach ensures a ground truth (i.e. the original 2D MR image) it is not directly applicable to *in vivo* MR data. The algorithm presented in this study overcomes these limitations and takes the spatially varying sensitivity of the MR receiver coils into consideration during image reconstruction and it can reconstruct data obtained at arbitrary sampling locations. Therefore, it can be applied to any *in vivo* 3D MR data acquisition.

In Pejoski *et al* (2015) a shearlet-based reconstruction algorithm was used that compares to our proposed method with W being the identity, i.e. no use of reweighting and applying fixed L1 regularization. Further, the experiments carried out in Pejoski *et al* (2015) are only applied to Cartesian sampling patterns (random point samples and radial lines on a grid). The approach in Pejoski *et al* (2015) can be combined with TGV as an additional regularizer which is the proposed method in Guo *et al* (2014) and a detailed experimental study using

Table 1. Image evaluation from clinical reviewers.

Reviewer 1	itSENSE	WaveCS	TV	3DShearCS
Diagnostic quality	16/20	17/20	16/20	16/20
Image score	1.15	1.15	1.2	1.2
Agreement with reference image	5/20	7/20	3/20	15/20
Reviewer 2	itSENSE	WaveCS	TV	3DShearCS
Diagnostic quality	15/20	16/20	17/20	18/20
Image score	1.0	1.05	1.05	1.4
Agreement with reference image	0/20	1/20	5/20	14/20

subsampled Cartesian data of FFT transformed 2D MR images was shown. In Liu *et al* (2017b) and Yazdanpanah and Regentova (2017) different TV regularizers were also considered instead of TGV for 2D data obtained by applying the FFT to existing 2D MR images. Our method only uses one regularizer and the image reconstruction quality is improved by the reweighting technique. Further, our main study is based on 3D MR data obtained from RPE lines.

We compared our proposed scheme to two widely used reconstruction approaches, regularization using wavelet-based and finite difference-based sparsity. Nevertheless, there are several other approaches such as second order total generalized variation which have also been reported to provide excellent image quality, which we did not compare against in this work (Knoll *et al* 2011).

Relative error and HaarPSI are commonly used image metrics but they only describe the difference to a reference image, without providing any information if the measured difference improves or decreases the image quality. This limitation can be seen in figure 10 for $R = 4$. The reference image is itSENSE with $R = 4$ and HaarPSI and the relative error suggest that TV, WaveCS and 3DShearCS perform worse than itSENSE for $R = 4$. Nevertheless, the images in figures 6 and 7 and the image quality metrics in figure 10 indicate that especially TV and 3DShearCS lead to a better image quality than itSENSE.

MR data acquisition used in this study provided 3D whole-heart images used for assessment of the morphology of the entire heart and was not specifically designed for the assessment of the coronary arteries. Nevertheless, the coronary arteries provided a sensitive measure to compare image quality between different methods.

The performance of 3DShearCS depends on the resolution of the images. Optimal results for a 3D shearlet system can only be achieved with high isotropic resolution and isotropic number of pixels. Here we used a 3D non-Cartesian trajectory which is specifically designed to fulfill this requirement. For other MR sampling schemes which provide anisotropic image data, for instance if the dimension in one direction is significantly smaller than the other two and those are very large, a 2D shearlet approach should be considered.

Another optimization option for the reconstruction is the shearlet filter. Depending on the data and the experimental setup the filter can be adapted to the image content. For instance, in vessel wall imaging more focus could be put on the edges, hence, smaller filters with more spatial localization may perform better than filters with large support.

The proposed reweighting approach could also be applied to 3D wavelet transforms, but only a 3D redundant wavelet transform would significantly benefit from the reweighting scheme which, to the best of our knowledge, is not available for Matlab. In addition, previously proposed WaveCS approaches do not use 3D redundant wavelet transform and therefore we compared 3DShearCS to a wavelet-based CS without iterative reweighting.

One of the main challenges of advanced MR image reconstruction approaches are reconstruction times. For this study the reconstruction times were 4 h on a 2 x Intel Xeon X2630v2 Hexa-Core machine with 64 GB memory. However, the code is also not optimized for speed but will be as a part of future work. A GPU-based implementation would reduce the reconstruction times greatly.

All the image reconstruction techniques used in this work required data dependent reconstruction parameters which had to be manually set by visually evaluating the image quality for a range of parameter. For all reconstruction approaches the number of iterations is an important parameters. For TV the number of iterations and the weighting of the regularization had to be adapted for different undersampling factors. For 3DShearCS the same set of reconstruction parameters was used for all *in vivo* experiments. The TV based-reconstruction required a change of parameters for different undersampling factors.

6. Conclusion

We have presented a novel CS reconstruction approach using shearlet-based sparsity transforms which can be used for arbitrary MR sampling patterns and exploits the information from multiple receiver coils to improve the conditioning of the reconstruction problem. An iterative reweighting approach is used to ensure fast convergence

of the algorithm and high image quality even for a low number of iterations, improving both the accuracy of the approach while reducing reconstruction times. The proposed 3DShearCS method was evaluated in 3D *in vivo* cardiac MR scans of healthy volunteers. Compared to existing reconstruction methods, 3DShearCS lead to superior image quality which was determined using standard image quality metrics and assessments of clinical experts. 3DShearCS ensures high quality 3D MR images with high isotropic resolution in short scan times and could help to promote 3D high-resolution CMR in clinical practice.

Acknowledgments

This work was done when J Ma was affiliated with the Technische Universität Berlin, he acknowledges support from the DFG Collaborative Research Center TRR 109 ‘Discretization in Geometry and Dynamics’ and the Berlin Mathematical School. G Kutyniok acknowledges partial support by the Einstein Foundation Berlin, Einstein Center for Mathematics Berlin (ECMath), DFG CRC/TR 109 ‘Discretization in Geometry and Dynamics’, DFG CRC 1114 ‘Scaling Cascades in Complex Systems’, RTG DAEDALUS (RTG 2433) and DFG SPP 1798 ‘Compressed Sensing in Information Processing’. G Kutyniok, J Schulz-Menger and T Schaeffter acknowledge support by RTG BIOQIC (RTG 2260).

References

- Ahmad R and Schniter P 2015 Iteratively reweighted ℓ_1 approaches to sparse composite regularization *IEEE Trans. Comput. Imaging* **1** 220–35
- Block K T, Uecker M and Frahm J 2007 Undersampled radial MRI with multiple coils. Iterative image reconstruction using a total variation constraint *Magn. Reson. Med.* **57** 1086–98
- Boubertakh R, Prieto C, Batchelor P G, Uribe S, Atkinson D, Eggers H, Sørensen T S, Hansen M S, Razavi R S and Schaeffter T 2009 Whole-heart imaging using undersampled radial phase encoding (RPE) and iterative sensitivity encoding (SENSE) reconstruction *Magn. Reson. Med.* **62** 1331–7
- Candès E J 2008 The restricted isometry property and its implications for compressed sensing *C. R. Math. Acad. Sci. Paris* **346** 589–92
- Candès E J and Donoho D L 2002 New tight frames of curvelets and optimal representations of objects with piecewise C^2 -singularities *Commun. Pure Appl. Math.* **57** 219–66
- Candès E J, Eldar Y C, Needell D and Randall P 2011 Compressed sensing with coherent and redundant dictionaries *Appl. Comput. Harmon. Anal.* **31** 59–73
- Candès E J, Romberg J K and Tao T 2005 Stable signal recovery from incomplete and inaccurate measurements *Commun. Pure Appl. Math.* **59** 1207–23
- Candès E J, Romberg J K and Tao T 2006 Robust uncertainty principles: exact signal reconstruction from highly incomplete frequency information *IEEE Trans. Inf. Theory* **52** 489–509
- Candès E J, Wakin M B and Boyd S P 2008 Enhancing sparsity by reweighted ℓ_1 minimization *J. Fourier Anal. Appl.* **14** 877–905
- Cruz G, Atkinson D, Buerger C, Schaeffter T and Prieto C 2016 Accelerated motion corrected three-dimensional abdominal MRI using total variation regularized SENSE reconstruction *Magn. Reson. Med.* **75** 1484–98
- Daubechies I 1992 *Ten Lectures on Wavelets* (CBMS-NSF Regional Conference Series in Applied Mathematics vol 61) (Philadelphia: SIAM) (<https://doi.org/10.1137/1.9781611970104>)
- Deng W and Yin W 2016 On the global and linear convergence of the generalized alternating direction method of multipliers *J. Sci. Comput.* **66** 889–916
- Donoho D L 2001 Sparse components of images and optimal atomic decomposition *Constr. Approx.* **17** 353–82
- Donoho D L 2006 Compressed sensing *IEEE Trans. Inf. Theory* **52** 1289–306
- Eckstein J and Bertsekas D P 1992 On the Douglas–Rachford splitting method and the proximal point algorithm for maximal monotone operators *Math. Program.* **55** 293–318
- Etienne A, Botnar R M, Muiswinkel A M C V, Boesiger P, Manning W J and Stuber M 2002 ‘Soap-Bubble’ visualization and quantitative analysis of 3D coronary magnetic resonance angiograms *Magn. Reson. Med.* **48** 658–66
- Feng L, Coppo S, Piccini D, Yerly J, Lim R P, Masci P G, Stuber M, Sodickson D K and Otazo R 2018 5D whole-heart sparse MRI *Magn. Reson. Med.* **79** 826–38
- Feng L, Srichai M B, Lim R P, Harrison A, King W, Adluru G, Dibella E V R, Sodickson D K, Otazo R and Kim D 2013 Highly accelerated real-time cardiac cine MRI using k-t SPARSE-SENSE *Magn. Reson. Imaging* **70** 64–74
- Forman C, Piccini D, Grimm R, Hutter J, Hornegger J and Zenge M O 2014 High-resolution 3D whole-heart coronary MRA: a study on the combination of data acquisition in multiple breath-holds and 1D residual respiratory motion compensation *MAGMA* **27** 435–43
- Gabay D and Mercier B 1976 A dual algorithm for the solution of nonlinear variational problems via finite element approximation *Comput. Math. Appl.* **2** 17–40
- Griswold M A, Jakob P M, Heidemann R M, Nittka M, Jellus V, Wang J, Kiefer B and Haase A 2002 Generalized autocalibrating partially parallel acquisitions (GRAPPA) *Magn. Reson. Med.* **47** 1202–10
- Guo K, Kutyniok G and Labate D 2006 Sparse multidimensional representations using anisotropic dilation and shear operators *Wavelets and Splines: Athens, GA 2005* vol 1 (Nashville, TN: Nashboro Press) pp 189–201
- Guo W, Qin J and Yin W 2014 A new detail-preserving regularity scheme *SIAM J. Imaging Sci.* **7** 1309–34
- Jackson J I, Meyer C H, Nishimura D G and Macovski A 1991 Selection of a convolution function for Fourier inversion using gridding *IEEE Trans. Med. Imaging* **10** 473–8
- Jung H, Sung K, Nayak K S and Ye J C 2009 k-t FOCUSS: a general compressed sensing framework for high resolution dynamic MRI *Magn. Reson. Med.* **1** 103–16
- Kido T, Kido T, Nakamura M, Watanabe K, Schmidt M, Forman C and Mochizuki T 2016 Compressed sensing real-time cine cardiovascular magnetic resonance: accurate assessment of left ventricular function in a single-breath-hold *J. Cardiovasc. Magn. Reson.* **18** 50
- Kittipoom P, Kutyniok G and Lim W Q 2012 Construction of compactly supported shearlet frames *Constr. Approx.* **35** 21–72

- Knoll F, Bredies K, Pock T and Stollberger R 2011 Second order total generalized variation (TGV) for MRI *Magn. Reson. Med.* **65** 480–91
- Kolbitsch C, Prieto C, Smink J and Schaeffter T 2011 Highly efficient whole-heart imaging using radial phase encoding-phase ordering with automatic window selection *Magn. Reson. Med.* **66** 1008–18
- Kutyniok G and Labate D 2012 Introduction to shearlets *Shearlets (Applied and Numerical Harmonic Analysis)* (New York: Springer) pp 1–38
- Kutyniok G and Lim W Q 2011 Compactly supported shearlets are optimally sparse *J. Approx. Theory* **163** 1564–89
- Kutyniok G and Lim W Q 2018 Optimal compressive imaging of fourier data **11** 507–46
- Kutyniok G, Lemvig J and Lim W Q 2012 Optimally sparse approximations of 3D functions by compactly supported shearlet frames *SIAM J. Math. Anal.* **44** 2962–3017
- Kutyniok G, Lim W Q and Reisenhofer R 2016 ShearLab 3D: faithful digital shearlet transforms based on compactly supported shearlets *ACM Trans. Math. Softw.* **42**
- Labate D, Lim W Q, Kutyniok G and Weiss G 2005 Sparse multidimensional representation using shearlets *Proc. SPIE* **5914** 254–62
- Liang D, Liu B, Wang J and Ying L 2009 Accelerating SENSE using compressed sensing *Magn. Reson. Med.* **62** 1574–84
- Lim W Q 2010 The discrete shearlet transform: a new directional transform and compactly supported shearlet frames *IEEE Trans. Image Process.* **19** 1166–80
- Lim W Q 2013 Nonseparable shearlet transform *IEEE Trans. Image Process.* **22** 2056–65
- Liu J, Feng L, Shen H W, Zhu C, Wang Y, Mukai K, Brooks G C, Ordovas K and Saloner D 2017a Highly-accelerated self-gated free-breathing 3D cardiac cine MRI: validation in assessment of left ventricular function *Magn. Reson. Mater. Phys. Biol. Med.* **30** 337–46
- Liu R W, Shi L, Yu S C H and Wang D 2017b Hybrid regularization for compressed sensing MRI: exploiting shearlet transform and group-sparsity total variation *20th Int. Conf. on Information Fusion (Fusion)* pp 1–87
- Lustig M, Donoho D L, Santos J M and Pauly J M 2008 Compressed sensing MRI *IEEE Signal Process. Mag.* **25** 72–82
- Ma J 2017 Generalized sampling reconstruction from Fourier measurements using compactly supported shearlets *Appl. Comput. Harmon. Anal.* **42** 294–318
- Miao X, Lingala S G, Guo Y, Jao T, Usman M, Prieto C and Nayak K S 2016 Accelerated cardiac cine MRI using locally low rank and finite difference constraints *Magn. Reson. Imaging* **34** 707–14
- Nakamura M, Kido T, Kido T, Watanabe K, Schmidt M, Forman C and Mochizuki T 2018 Non-contrast compressed sensing whole-heart coronary magnetic resonance angiography at 3T: a comparison with conventional imaging *Eur. J. Radiol.* **104** 43–8
- Otazo R, Kim D, Axel L and Sodickson D K 2010 Combination of compressed sensing and parallel imaging for highly accelerated first-pass cardiac perfusion MRI *Magn. Reson. Imaging* **64** 767–76
- Pang J, Bhat H, Sharif B, Fan Z, Thomson L E J, Labounty T, Friedman J D, Min J, Berman D S and Li D 2014 Whole-heart coronary MRA with 100% respiratory gating efficiency: self-navigated three-dimensional retrospective image-based motion correction (TRIM) *Magn. Reson. Imaging* **71** 67–74
- Pejoski S, Kafedziski V and Gleich D 2015 Compressed sensing MRI using discrete nonseparable shearlet transform and FISTA *IEEE Signal Process. Lett.* **22** 1566–70
- Piccini D et al 2014 Respiratory self-navigated postcontrast whole-heart coronary MR angiography: initial experience in patients *Radiology* **270** 378–86
- Prothmann M et al 2016 High spatial resolution cardiovascular magnetic resonance at 7.0 Tesla in patients with hypertrophic cardiomyopathy—first experiences: lesson learned from 7.0 tesla *PLoS One* **11** 1–13
- Pruessmann K P, Weiger M, Boernert P and Boesiger P 2001 Advances in sensitivity encoding with arbitrary k-space trajectories *Magn. Reson. Med.* **46** 638–51
- Pruessmann K P, Weiger M, Scheidegger M B and Boesiger P 1999 SENSE: sensitivity encoding for fast MRI *Magn. Reson. Imaging* **42** 952–62
- Ramani S and Fessler J A 2010 Parallel mr image reconstruction using augmented lagrangian methods *IEEE Trans. Med. Imaging* **30** 694–706
- Ramani S and Fessler J A 2011 Regularized parallel MRI reconstruction using an alternating direction method of multipliers *Proc. IEEE Int. Symp. Biomedical Imaging* pp 385–8
- Ravishankar S and Bresler Y 2011 MR image reconstruction from highly undersampled k-space data by dictionary learning *IEEE Trans. Med. Imaging* **30** 1028–41
- Reisenhofer R, Bosse S, Kutyniok G and Wiegand T 2018 A haar wavelet-based perceptual similarity index for image quality assessment *Signal Process. Image Commun.* **61** 33–43
- Shannon C E 1948 A mathematical theory of communication *Bell Syst. Tech. J.* **27** 623–56
- Sodickson D K and Manning W J 1997 Simultaneous acquisition of spatial harmonics (SMASH): fast imaging with radiofrequency coil arrays *Magn. Reson. Imaging* **38** 591–603
- Uecker M, Lai P, Murphy M J, Virtue P, Elad M, Pauly J M, Vasanawala S S and Lustig M 2014 ESPRiT—an eigenvalue approach to autocalibrating parallel MRI: where SENSE meets GRAPPA *Magn. Reson. Imaging* **71** 990–1001
- Vincenti G et al 2014 Compressed sensing single-breathhold CMR for fast quantification of LV function, volumes, and mass *JACC Cardiovasc. Imaging* **7** 882–92
- Yazdanpanah A P and Regentova E E 2017 Compressed sensing magnetic resonance imaging based on shearlet sparsity and nonlocal total variation *J. Med. Imag.* **4**